PERGAMON

Vacuum 60 (2001) 339–346

VACUUM
SURFACE ENGINEERING, SURFACE INSTRUMENTATION & VACUUM TECHNOLOGY

www.elsevier.nl/locate/vacuum

Mechanical and surface analysis of $Ti_{0.4}Al_{0.6}N$/Mo multilayers

C.J. Tavares[a,*], L. Rebouta[a], M. Andritschky[a], F. Guimarães[b], A. Cavaleiro[c]

[a]*Departamento de Física, Universidade do Minho, Campus de Azurém, 4800-058 Guimarães, Portugal*
[b]*IMAT, Universidade do Minho, 4700-320 Braga, Portugal*
[c]*ICMES, F.C.T da Universidade de Coimbra, 3030 Coimbra, Portugal*

Received 18 May 2000; received in revised form 20 July 2000; accepted 31 July 2000

Abstract

The quest for hard materials that are able to sustain elevated stresses as tools or cutting processes has led to the investigation of (Ti,Al)N/Mo multilayer coatings. These structures have been deposited by dc magnetron sputtering on high-speed steel and stainless-steel substrates and designed with modulation periods of approximately 13 nm, up to a total thickness of 2.8 μm. Experimental X-ray diffraction (XRD) achieved the basics involving structural quality and texture while RBS provided the composition. From AFM observations the waviness of the surface was monitored and it was found that the rms roughness values were minimised for a bias voltage of −120 V. Ultramicrohardness values of 33 GPa were obtained for the best samples, and their adhesion to the steel substrates was also studied. Residual stress measurements revealed a compressive stress state that prevailed in these structures, ranging from −0.2 to −1.3 GPa.

Keywords: Multilayers; AFM; Ultramicrohardness; Adhesion; Residual stress; Roughness

1. Introduction

The successful application of hard coatings as wear protection relay on an optimised combination of physical and mechanical properties of the coating constituents. Multilayers are one-dimensional synthetic structures comprising a number of alternate layers. They are used in a vast range of applications [1,2]. Wear prevention on steel tools in cutting applications is our major interest while attempting to produce (Ti,Al)N/Mo coatings. Recently, some publications mention the fact that multilayers endow for tribological applications owing to their elevated hardness and strength [3–7]. This improvement is credited to the presence of more interfaces that results in crack deflection, thereby dissipating more energy and enhancing toughness. From a functional standpoint, chemical stability, hardness and good adhesion to the substrates is essential. Optimum coating thickness, fine grain microstructures and a compressive residual stress can further enhance the multilayer's performance [6]. Both $Ti_{0.4}Al_{0.6}N$ (fcc) and Mo (bcc) possess a cubic crystal structure and have similar properties, such as high melting point, good chemical and thermal stabilities and comparable elastic properties.

* Corresponding author. Tel.: +351-253-510154; fax: +351-253-510153.

E-mail address: ctavares@fisica.uminho.pt (C.J. Tavares).

0042-207X/01/$ - see front matter
PII: S0042-207X(00)00413-9

2. Experimental details

(Ti,Al)N/Mo coatings were deposited using a custom-made sputtering system. An Ar/N_2 enriched atmosphere was present in the chamber, with an argon flow rate (pressure) of 140 cm^3/min (0.35 Pa) and a nitrogen flow rate of 8.4 cm^3/min (0.13 Pa) for growing $Ti_{0.4}Al_{0.6}N$, while to produce Mo the Ar flow was varied from 160 to 250 cm^3/min (0.6 to 0.7 Pa). Pure 200 mm × 100 mm × 6 mm TiAl and Mo targets were used. A current of approximately 0.01 A/cm^2 was applied to both magnetrons. The substrate bias voltage was changed from -60 to -120 V while the target-to-substrate distance was kept at 110 mm in all depositions. A typical base pressure of the order of 5×10^{-5} Pa was achieved, and the substrate temperature during deposition was approximately 200°C. Before deposition the substrates were in situ sputter-etched in an argon atmosphere of 7 Pa with a dc power of 100 W during 20 min. The samples were grown on 30 mm in diameter, 5 mm thick, high-speed steel (AISI M2) discs and 25 mm in diameter, 0.5 mm thick, stainless-steel (AISI 316) discs.

Rutherford Backscattering Spectrometry (RBS) determined the film composition. A 2 MeV He^+ beam in a 3.0 MV Van de Graaff accelerator was used [8]. The backscattered particles were detected by a surface barrier detector placed at 160° to the beam direction in the Cornell geometry and with an energy resolution FWHM of 14 keV. Afterwards, the RBS spectra were fitted with Rump code [9].

A Digital Instruments NanoScope III atomic force microscope (AFM), working in tapping mode, was employed to study the surface morphology of these coatings. For the XRD scans a Philips PW3040/00 X'Pert diffractometer was used in the standard Bragg-Brentano geometry. In the low-angle regime, the length scales that are probed are greater than the lattice spacing of the constituent layers. Therefore, the scattering solely arises from the chemical modulation of the structure. The modulation period can be experimentally assessed through the position of the low-angle Bragg diffraction peaks [10,11]:

$$n = \frac{2\Lambda}{\lambda}\sqrt{\cos^2(\theta_c) - \cos^2(\theta_n)}. \quad (1)$$

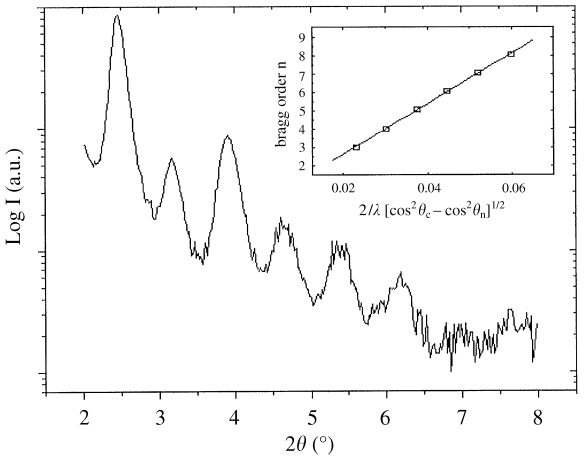

Fig. 1. Low-angle diffraction pattern for sample DB1 showing Bragg peaks up to the eighth order. Through the position of these peaks and by applying Eq. (1) it is possible to derive the multilayer periodicity (see inset).

n represents the order of diffraction related to the Bragg peak positioned at θ_n, Λ is the modulation periodicity, λ corresponds to the Co K_α X-ray wavelength,and $\theta_c \approx 0.4°$ is the critical angle below which the radiation is totally reflected. In Fig. 1 an example of this is given (for sample DB1) where the position of the Bragg peaks is plotted as a function of $(2/\lambda)\sqrt{\cos^2(\theta_c) - \cos^2(\theta_n)}$; through the slope the modulation period is derived.

Hardness testing enables a continuous monitoring of the load and depth of penetration experienced by the indenter during the indentation process. These depth-sensing measurements allow the estimation of not only the hardness but also Young's modulus [12,13]. The ultramicrohardness experiments were carried out on a computerised Fischerscope dynamic ultramicrohardness tester (H100 model), using a Vickers indenter and a maximum load of 30 mN.

An established method of assessing the adhesion of hard coatings made by PVD is the scratch test. The equipment used was a Sebastian-5A model from the Quad Group. A 200 μm radius diamond tip was used with the scratching speed being set at 0.0167 cm/s while the load rate was kept at 100 N/min. An analysis of the AE spectrum coupled with careful microscopic analysis of the scratch

tracks aids the task of identifying the value of the critical load (L_c) [13,14]. We consider L_c as the load at which the first adhesive failure mode occurs and it is clearly visible, regardless of the film remaining bonded after this incident along the segueing scratch track.

The technique used for residual stress measurement is based on the associated curvature deflection of a thin substrate [15,16]. The major advantages of this approach in comparison to the measurements of elastic strains in the films via XRD [17] resides in the fact that in the deflection method no information regarding the coating elastic properties is required to calculate the residual stress.

In Stoney's equation [18],

$$\sigma = -\frac{E_s}{6(1-v_s)} \times \frac{t_s^2}{t_c} \times [r_a^{-1} - r_b^{-1}]. \quad (2)$$

$E_s/(1-v_s)$ refers to the biaxial modulus of the stainless-steel substrate ($E_s = 215\,\text{GPa}$ and $v_s = 0.283$ [19]), t_s and t_c are, respectively, the thickness of the steel substrate and coating, and finally, the parameters r_b and r_a represent the radius of the curvatures of the substrates before and after deposition. By using the last expression one can quantitatively evaluate the residual stress inside the films. The curvature of the samples was analysed with a Mitutoyo CNC co-ordinate-measuring unit.

3. Results and discussion

Low-angle XRD scans provided us the modulation periodicity. Diverse Bragg peaks, associated with the low-angle patterns, was identified up to the eighth order. This allowed the precise determination of the modulation periodicity (Λ — see Table 1) with very low error, and also positively ensured a good chemical modulation while producing the multilayers. A good indicator of the reproducibility of these structures is that the modulation period was kept constant at approximately about 13 nm. High-angle XRD measurements provided texture information, for instance about its evolution with the bias voltage, which is shown in Fig. 2. From this

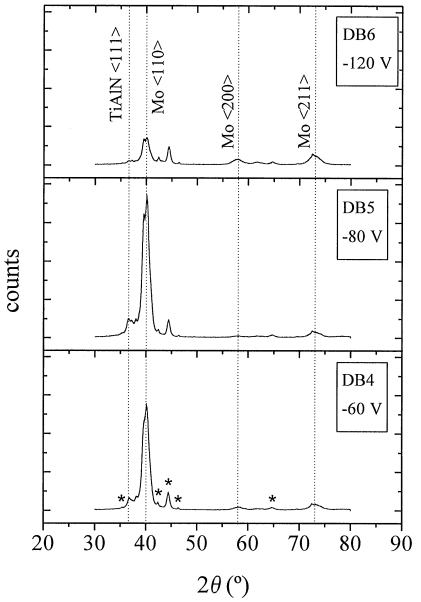

Fig. 2. High-angle diffraction patterns for samples DB4, DB5 and DB6, grown with $P^{Mo}(Ar) = 0.7\,\text{Pa}$, showing the texture evolution as the bias voltage increases from -60 to $-120\,\text{V}$. For intensity comparison, the same vertical scale is used. The peaks labelled with an asterisk correspond to the steel substrate.

Figure a change in the Mo texture as the bias voltage increases from -60 to $-120\,\text{V}$ is observed. Up to $-80\,\text{V}$ a strong Mo (1 1 0) texture is present, however at $-120\,\text{V}$ it is diminished and an enhancement of the (2 0 0) and (2 1 1) growth planes occur instead.

From AFM observations on all multilayered samples the corresponding rms roughness (R_a) was calculated from $5\,\mu\text{m} \times 5\,\mu\text{m}$ line scans; the results are presented in Table 1. In Fig. 3a, b and c these type of scans are shown for samples DB1, DB4 and DB5, respectively, while in Fig. 3d a smaller scan of $0.5\,\mu\text{m} \times 0.5\,\mu\text{m}$ from DB4 is given. In this figure it is possible to observe the dome-rounded shape, characteristic of these multilayer columnar grains. This feature on the surface results from the wavy rough interfaces and texture misorientation of the grains. While comparing Fig. 3b and Fig. 3c with the results in Table 1 one concludes that an increment of the bias voltage from -60 to $-80\,\text{V}$ enhances both values of disorder (R_a) and the columnar diameter. Additionally, while comparing

Table 1
Experimental details and calculated results regarding the deposition of different samples. Bias is the polarisation potential applied to the substrate holder and $P^{Mo}(Ar)$ the partial pressure of argon relative to the deposition of Mo. The values of $P^{TiAlN}(N_2)$ and $P^{TiAlN}(Ar)$ were kept constant on all depositions at 0.13 and 0.35 Pa, respectively. The modulation periodicity (Λ) was determined by applying Eq. (1). R_a stands for the rms roughness determined from the AFM analysis on a $5\,\mu m \times 5\,\mu m$ area

Sample	Type	$P^{Mo}(Ar)$ (Pa)	Λ (nm)	Bias (V)	R_a (nm)
DB 1	$(Ti_{0.4}Al_{0.6}N/Mo) \times 200$	0.6	13.6	− 60	7
DB 2	$(Ti_{0.4}Al_{0.6}N/Mo) \times 200$	0.6	13.6	− 80	11
DB 3	$(Ti_{0.4}Al_{0.6}N/Mo) \times 200$	0.6	11.0	− 120	6
DB 4	$(Ti_{0.4}Al_{0.6}N/Mo) \times 200$	0.7	13.6	− 60	10
DB 5	$(Ti_{0.4}Al_{0.6}N/Mo) \times 200$	0.7	12.8	− 80	14
DB 6	$(Ti_{0.4}Al_{0.6}N/Mo) \times 200$	0.7	11.0	− 120	6
$Ti_{0.4}Al_{0.6}N$	–	–	–	− 60	–
Mo	–	0.7	–	− 60	–

Fig. 3a and Fig. 3b a similar result was found as the working Ar pressure was elevated from 0.6 to 0.7 Pa, keeping the bias constant. It is well known that an increase in the working gas pressure corresponds to an enhancement of the wave profile of the surface that is being bombarded [20]. The exception to this trend is associated with the samples grown with a bias voltage of − 120 V where the R_a values and also the modulation period decrease substantially. A high-enough ion flux and subsequent higher surface mobility permits the atoms to stack with less roughness, while the decrease in the thickness was due to re-sputtering effects derived from the high voltage present in the substrate holder. Sample DB1 in (Fig. 3a) bears more surface defects than the others do; from Fig. 3b and c it is obvious how the film surface becomes cleaner with defects and protrusions as the bias voltage increases. The possible mechanism responsible for this has to do with the misorientation of columns during growth that often arise from grains exposing a higher surface energy to the deposition flux. From AFM images these protrusions can be at the most 350 nm wide and 300 nm high. The AFM roughness results correlate well with the observable texture changes referred to in the last paragraph with the assumption that the (1 1 0) island growth inhibits adatom mobility and therefore increases the overall roughness, whilst when increasing the bias to − 120 V the (2 0 0) and (2 1 1) growth direction surface energy is higher and hence we have less roughness. These results are in agreement with the previous published work wherein the low-angle XRD patterns were fitted with SUPREX and from those fits a value for the interfacial roughness was estimated [21]. The behaviour of the interfacial roughness with bias increment was the same, however these refined values were quite smaller compared to the R_a values due to the depth-sensing resolution of the X-rays, which is limited to the size of a grain whilst in the AFM measurements the lateral validity is much greater.

The ultramicrohardness experiments not only unveiled the hardness (*HV*) of these multilayers itself but also the Young's modulus (*E*). Figs. 4 and 5 shows these data as a function of the bias voltage. For different Mo sputtering conditions and for a $\Lambda \approx 13.5$ nm, both *HV* and *E* increase with the applied bias voltage up to maximum values of 33 and 440 GPa, respectively. This behaviour of *HV* and *E* with increasing bias voltage can be justified by the fact that the negative potential accelerates the gas ions to the growing coating and this additional supplied energy causes a coating densification and respective enhancement of the intrinsic compressive stress. This densification also contributes to the flattening of the surfaces; therefore lowers surface roughness.

Adhesion tests revealed critical loads (L_c) ranging from a minimum of 12 N, for the worst samples, up to 32 N, for the best ones; as shown in Fig. 6. The mechanism that is associated with these

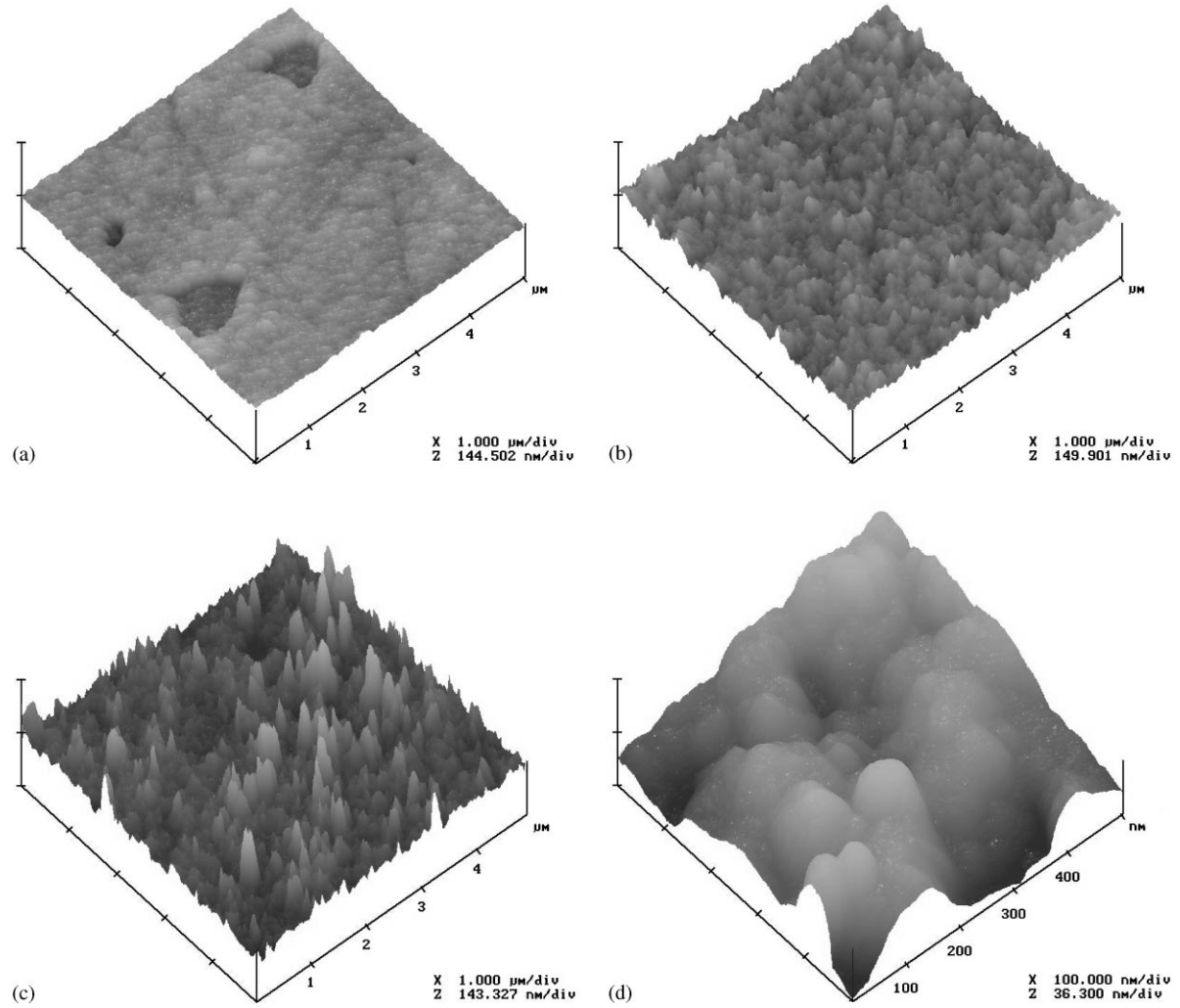

Fig. 3. Atomic force microscopy $5\,\mu m \times 5\,\mu m$ images of the morphology of samples: (a) DB1, (b) DB4 and (c) DB5. A smaller $0.5\,\mu m \times 0.5\,\mu m$ scan from DB4 is shown in (d).

critical loads and hence with adhesive failure is spallation, which occurs mainly laterally on the scratch track revealing the underlying substrate at the same time, which can be viewed in Fig. 7. Besides spallation, tensile cracks are also evident in the scratch track; however the coating remains fully adherent. These cracks result from tensile frictional forces on the trailing edge of the indenter, which balances the compressive frictional stresses ahead from the indenter. In Table 2 the L_c values for $Ti_{0.4}Al_{0.6}N$/Mo multilayers, bulk $Ti_{0.4}Al_{0.6}N$ and Mo are presented. Since the bulk Mo film adheres better than the best multilayer coating, further work has to be done on the optimisation of the growth of these structures. Nevertheless, the dependency of L_c with increasing bias is similar as with HV, E and σ. The relatively small change in the argon pressure while producing Mo did not influence the overall mechanical properties of these coatings.

All samples are under a compressive in-plane residual stress (σ), the majority ranging from

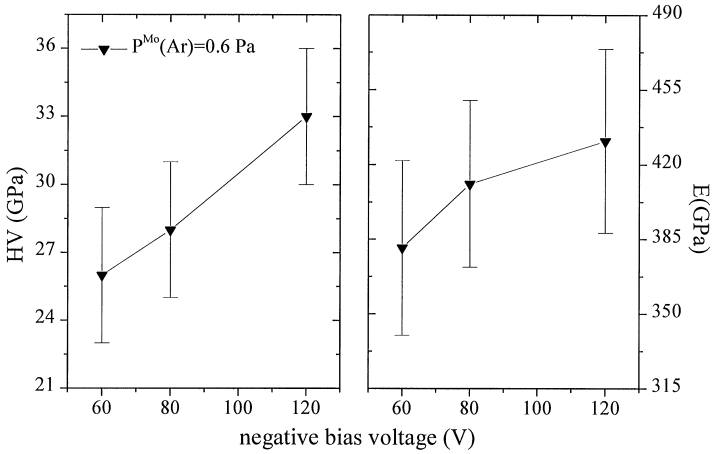

Fig. 4. Evolution of the ultramicrohardness (*HV*) and Young's modulus (*E*) with increasing bias voltage, for $[Ti_{0.4}Al_{0.6}N/Mo] \times 200$ samples grown with $P^{Mo}(Ar) = 0.6\,Pa$.

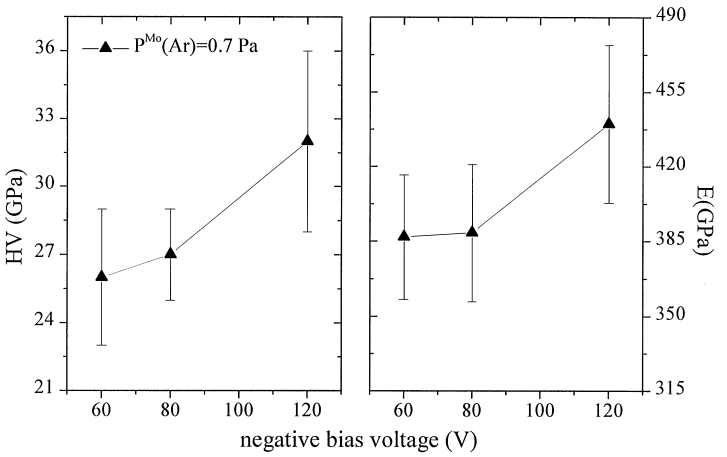

Fig. 5. Evolution of the ultramicrohardness (*HV*) and Young's modulus (*E*) with increasing bias voltage, for $[Ti_{0.4}Al_{0.6}N/Mo] \times 200$ samples grown with $P^{Mo}(Ar) = 0.7\,Pa$.

approximately -0.2 to -0.5 GPa. A couple of higher values of the order of -1 GPa for particular experimental conditions are related to a high (-120 V) polarisation voltage during deposition. From the results in Table 2 and Fig. 6 we conclude that both the increases of the bias voltage and to some limit, the argon partial pressure to produce Mo increase the relative residual stress values. Hence, the effect of the bias voltage as it is elevated from 0 to -120 V is to increase the state of residual stress on these coatings. The synergetic dependence of the stress field and hardness with increasing negative bias voltage can be explained by the fact that an increase in bias corresponds to another in ion bombardment. The collisional cascade effects associated with this enhance film densification and void annihilation; hence the strengthening and hardening effects [22–24].

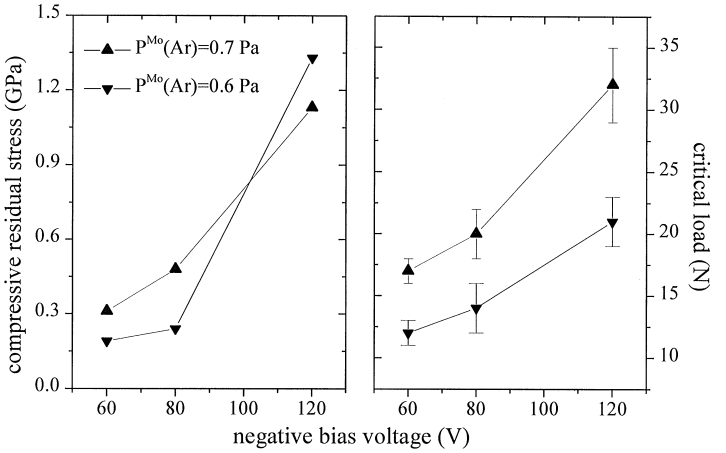

Fig. 6. Evolution of the negative (compressive) residual stress (σ) and adhesion failure load (L_c) with increasing bias voltage, for $[Ti_{0.4}Al_{0.6}N/Mo] \times 200$ samples grown with $P^{Mo}(Ar) = 0.6$ Pa and $P^{Mo}(Ar) = 0.7$ Pa.

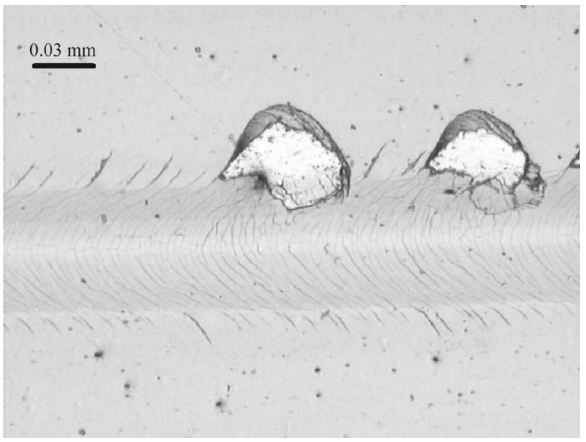

Fig. 7. Profile of an adhesion failure on a $[Ti_{0.4}Al_{0.6}N/Mo] \times 200$ sample (DB4) during critical load determination by means of a scratch test.

Table 2
Experimental results obtained for the multilayer $Ti_{0.4}Al_{0.6}N/Mo$ coatings (DB series) and for bulk $Ti_{0.4}Al_{0.6}N$ and Mo. *HV* refers to the Vickers ultramicrohardness, *E* the Young's modulus, L_c is the critical load and σ the residual stress in the thin film

Sample	*HV* (GPa)	*E* (GPa)	L_c (N)	σ (GPa)
DB 1	26 ± 3	381 ± 41	12 ± 1	-0.19
DB 2	28 ± 3	411 ± 39	14 ± 2	-0.24
DB 3	33 ± 3	431 ± 43	21 ± 2	-1.33
DB 4	26 ± 3	387 ± 29	17 ± 1	-0.31
DB 5	27 ± 2	389 ± 32	20 ± 2	-0.48
DB 6	32 ± 4	440 ± 37	32 ± 3	-1.13
$Ti_{0.4}Al_{0.6}N$	–	–	29 ± 1	-0.26
Mo	–	–	35 ± 2	-1.28

4. Conclusions

We report in this paper the production and mechanical characterisation of PVD-grown $Ti_{0.4}Al_{0.6}N/Mo$ multilayers. Indentation experiments yielded ultramicrohardness values as high as 33 GPa. While monitoring adhesion failures during scratch tests we witnessed that some coatings withhold critical loads up to 32 N. A strong spallation of film material from the interface with the substrate occurs at higher loads. By polarising the substrates with a negative potential one can control changes in surface morphology, columnar growth, roughness, and consequently the mechanical behaviour of these multilayers. With the AFM technique, we were able to determine the rms roughness and found that our coatings developed a dome-rounded surface structure during growth, similar to

the zone 1 microstructure of Thornton's model [25] for a lower bias of -60 V and gradually changing to zone T as the bias increased to -120 V.

References

[1] Ma KJ, Bloyce A, Bell T. Surf Coat Technol 1995;76–77:297.
[2] Donahue LA, Cawley J, Lewis DB, Brooks JS, Münz W-D. Surf Coat Technol 1995;76–77:149.
[3] Münz W-D. Surf Coat Technol 1993;58:20.
[4] Chu X, Barnett SA, Wong MS, Sproul WD. Surf Coat Technol 1993;57:13.
[5] Sundgren JE, Birch J, Kakansson G, Hultman L, Helmersson U. Thin Solid Films 1990;193–194:818.
[6] Santhanam AT, Quinto DT. In: Coteh CM, Sprague JA, Smidt FA Jr, editors. ASM handbook, Vol. 5: surface engineering. ASM International, 1996. p. 905.
[7] Quinto DT. J Vac Sci Technol 1998;A6:2149.
[8] Silva MF, Silva MR, Alves EJ, Melo AA, Soares JC, Winand J, Vianden R. In: Kossowsky R, Singhal S, editors. Surface engineering. NATO ASI, Nijhoff: Les Arcs, 1984. p. 74.
[9] Doolittle LR. Nucl Instr and Meth 1985;A9:344.
[10] Gu YS, Chai WP, Mai ZH, Zhao JG. Phys Rev B 1994;50:6119.
[11] Tavares CJ, Rebouta L, Almeida B, Sousa JB. Surf Coat Technol 1998;100–101:65.
[12] Pharr GM, Oliver WC. MRS Bulletin, July 28,1992.
[13] Tavares CJ, Rebouta L, Andritschky M, Ramos S. J Mat Proc Technol 1999;92–93:177.
[14] Burnett PJ, Rickerby DS. Thin Solid Films 1987;54:403.
[15] Larsson M, Hedenqvist P, Hogmark S. Surf Engng 1996;12(1):43.
[16] Kumagai HY. 9th International Conference on CVD. The Electrochem Soc 1984. p. 189.
[17] Perry AJ. J Vac Sci Technol 1990;A8(3):1351.
[18] Stoney GG. Proc R Soc London 1909;A82:172.
[19] Smithels CJ. Metals reference book, 5th ed. London: Butterworth, 1976. p. 975.
[20] Fullerton EE, Schuller IK, Bruynseraede Y. MRS Bulletin, December 33, 1992.
[21] Tavares CJ, Rebouta L, Alves EJ. Thin Solid Films 2000;373(1–2):287.
[22] Petrov I, Hultman L, Sundgren J-E, Greene JE. J Vac Sci Technol 1992;A10:265.
[23] Chu X, Barnett S. J Appl Phys 1995;77(9):4403.
[24] Rickerby DS. J Vac Technol 1986;A4:2809.
[25] Thornton JA. J Vac Technol 1986;A4:3059.